Supplementary material: The interplay between topological defects and CO_2 and NH_3 adsorption in graphene

Daniel Moreno-Rodríguez [1,*], Eva Scholtzová [2], Hirotomo Nishihara [3,4,*]

[1] Department of Mechanical and Aerospace Engineering, Sapienza University of Rome. Via Eudossiana 18, 00184 Rome, Italy

[2] Institute of Inorganic Chemistry, Slovak Academy of Science, Dúbravská cesta 9, 84536 Bratislava, Slovakia

[3] Institute of Multidisciplinary Research for Advanced Materials, Tohoku University, 2-1-1, Katahira, Aoba-ku, Sendai, 980-8577, Japan

[4] Advanced Institute for Materials Research (WPI-AIMR), Tohoku University, 2-1-1, Katahira, Aoba-ku, Sendai, 980-8577, Japan

(*) daniel.morenorodriguez@uniroma1.it ; hirotomo.nishihara.b1@tohoku.ac.jp

CO_2-G

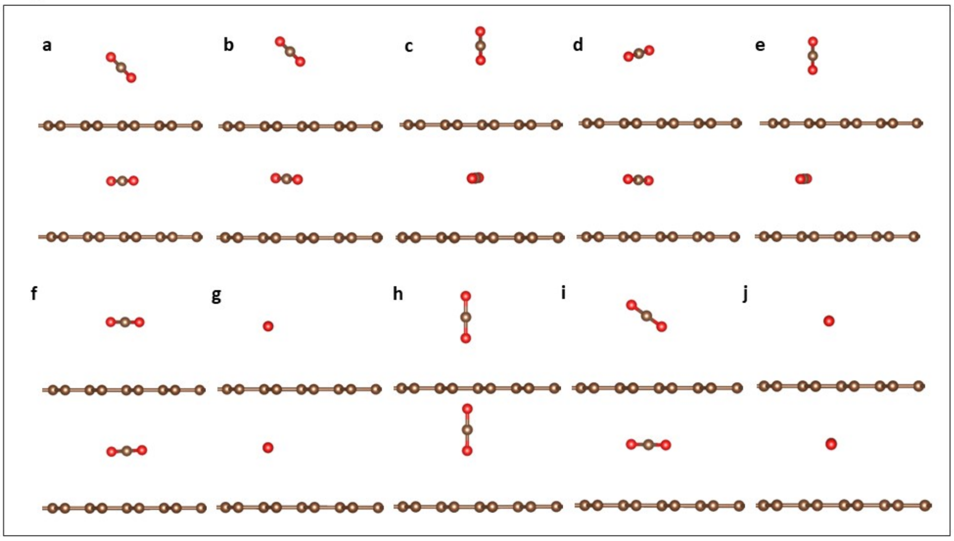

NH_3-G

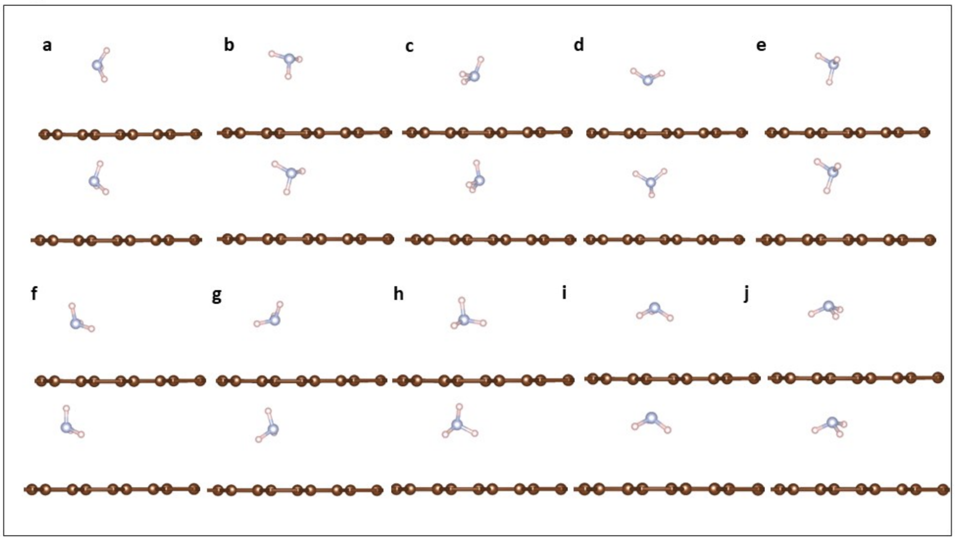

CO_2-MG7

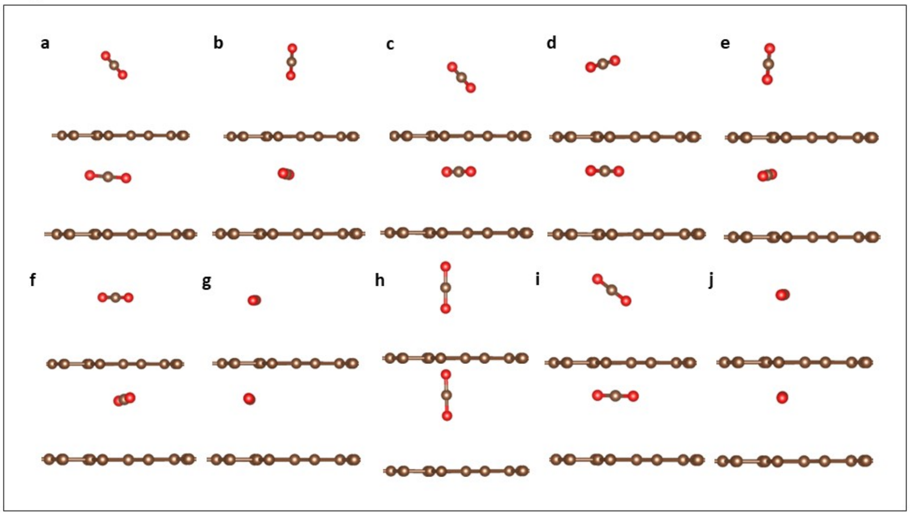

NH_3-MG7

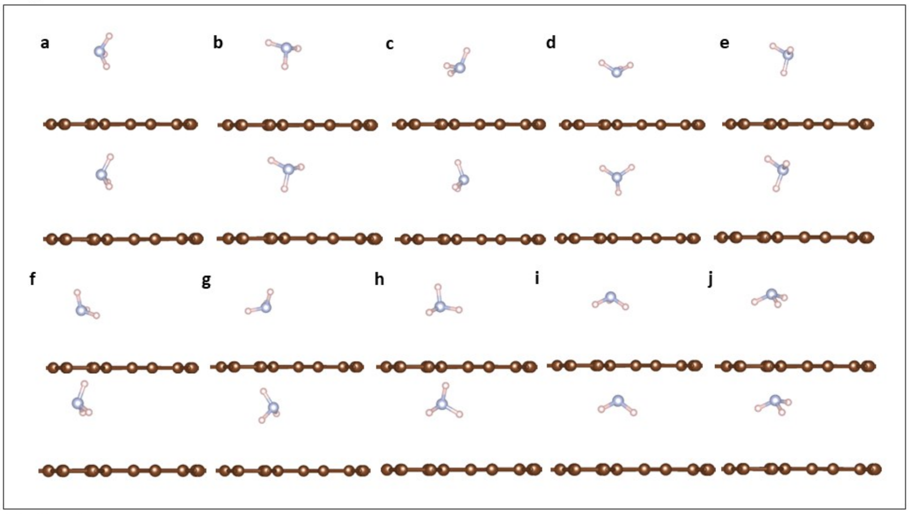

CO_2-MG8

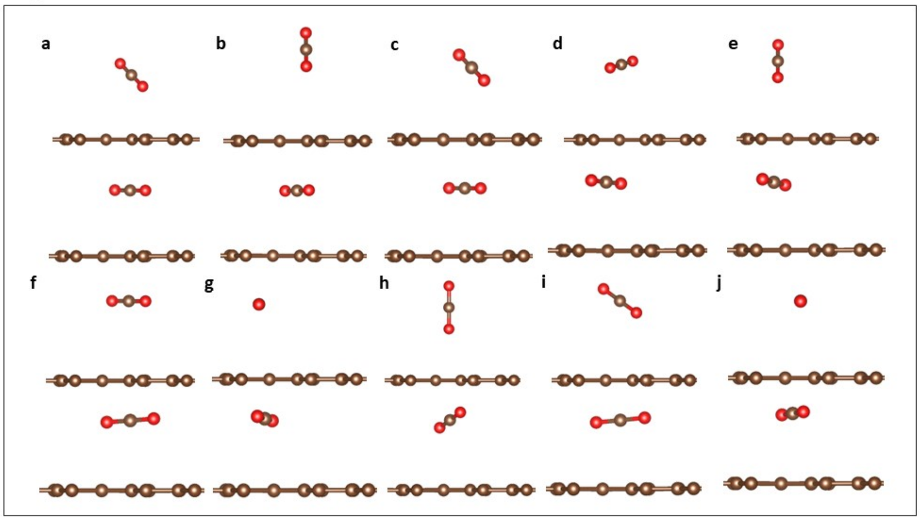

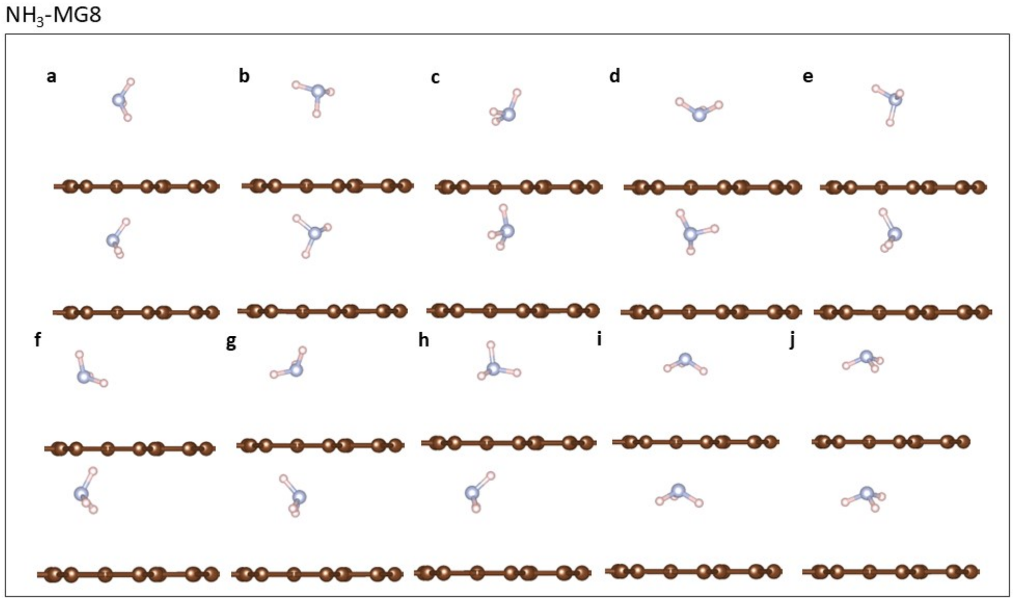

Figure S1. Initial adsorption configurations of CO_2 and NH_3 on pristine graphene (CO_2/ NH_3–G), graphene with 5-7-membered rings (CO_2/NH_3–MG7), and graphene with 5-8-membered rings (CO_2/NH_3–MG8). Ten representative orientations and adsorption sites (a–j) were considered as starting geometries for structural optimization for each combination. The initial setting is on top, while the relaxed model is on the bottom. Calculations were performed with DFT-D3 using a 5×5×1 Monkhorst-Pack grid and convergence thresholds of 10^{-6} eV (energy) and 0.01 eV/Å (forces).

Figure S2. Total energies (TOTEN, top panels) and adsorption energies (AE, bottom panels) for CO_2 (left) and NH_3 (right) across different initial adsorption configurations (a–j) on pristine graphene (G), MG7, and MG8. Only configurations yielding negative adsorption energies (favourable adsorption) are shown, while positive AE values were not included. The lowest-energy configurations, discussed in the main text, were identified from these comparisons.

Defect formation:

The MG7 model corresponds to a Stone–Wales defect, formed by a 90° rotation of a C–C bond that converts four hexagons into two pentagons and two heptagons. This transformation, while topologically simple, involves overcoming a large activation barrier (~10 eV), meaning that under equilibrium conditions it is improbable without external stimuli such as electron irradiation, mechanical strain, or rapid quenching [1, 2]. Once formed, SW defects typically have formation energies (E_f) of 5.0–7.5 eV, depending on computational approach and degree of out-of-plane buckling, which can relieve in-plane stress by hundreds of meV [2]. Our calculated value of 4.685 eV lies slightly below this range, which we attribute to the allowance for full structural relaxation (including buckling) and finite-size effects in our supercell that facilitate strain release.

The MG8 model is a reconstructed divacancy featuring adjacent five- and eight-membered rings, consistent with the 5–8–5 defect motif. Such defects originate from the removal of two adjacent carbon atoms, producing an unstable divacancy that reconstructs via bond rotations and rehybridization into a more stable configuration [3, 4]. Literature values for reconstructed divacancies typically range from 7.0–13.0 eV, with the precise number depending on the reconstruction type (5–8–5 or 555–777) and local strain conditions [3]. Our calculated E_f value of 4.983 eV is notably lower, which can be rationalized by the fact that the MG8 structure in our model arises within a pre-strained lattice in a smaller periodic cell. This context enables greater strain sharing between defect images. It promotes out-of-plane relaxation, both of which reduce the incremental energy required to form the defect compared to an isolated case in pristine graphene.

Defect formation energies E_f were computed as

$$E_f = E_{def} - E_{prist} + n\,\mu_C$$

where E_{def} and E_{prist} are the total energies of the defect-containing and pristine supercells, n is the number of removed carbon atoms, and μ_C is the carbon chemical potential taken as the energy per C atom of the pristine 64-atom and 48-atom graphene cells (i.e. -9.31 eV for both cases). For topology-conserving defects (e.g., MG7) n=0.

Defect (model)	**E_f (eV/defect)**	**Literature values (eV/defect)**
Stone–Wales (SW) MG7	4.685	5.0 – 7.5 [1, 2]
Divacancy 5–8–5 (MG8)	4.983	7.0 – 13.0 [3, 4]

Table S1. Defect formation energies for MG7 and MG8 models

[1] Banhart, F.; Kotakoski, J.; Krasheninnikov, A. V. Structural defects in graphene. ACS Nano 2011, 5 (1), 26–41. https://doi.org/10.1021/nn102598m.

[2] Skowron, S. T.; Lebedeva, I. V.; Popov, A. M.; Bichoutskaia, E. Energetics of atomic scale structure changes in graphene. Chem. Soc. Rev. 2015, 44, 3143–3176. https://doi.org/10.1039/C4CS00499J.

[3] Bhatt, M. D.; Kim, H.; Kim, G. Various defects in graphene: a review. RSC Adv. 2022, 12, 19043–19068. https://doi.org/10.1039/D2RA02540A.

[4] Lherbier, A.; Dubois, S. M.-M.; Declerck, X.; Niquet, Y.-M.; Roche, S.; Charlier, J.-C. Transport properties of graphene containing structural defects. Phys. Rev. B 2012, 86, 075402. https://doi.org/10.1103/PhysRevB.86.075402.

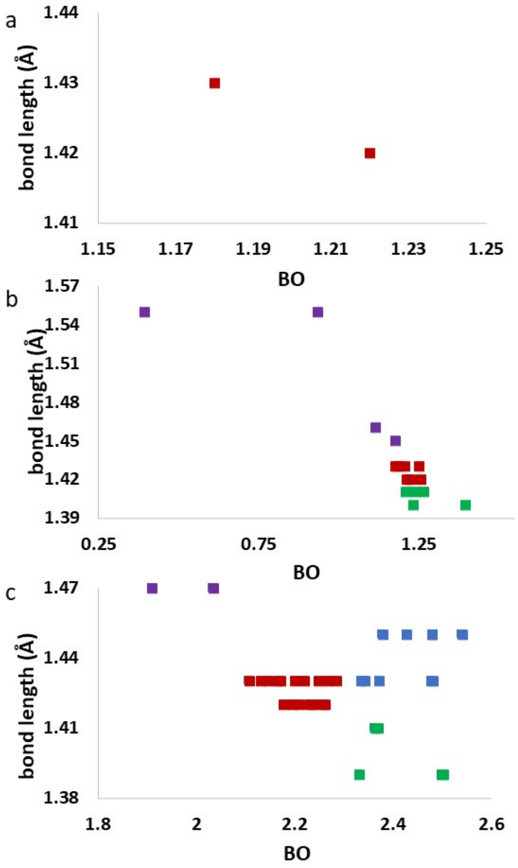

Figure S3. Bond lengths and bond orders (BO) for the G (a), MG7 (b) and MG8 (c) models. The coloured dots represent the different groups of bonds found in 6-membered rings (a), 5-6-7-membered rings (b) and 5-6-7-8-membered rings (c).

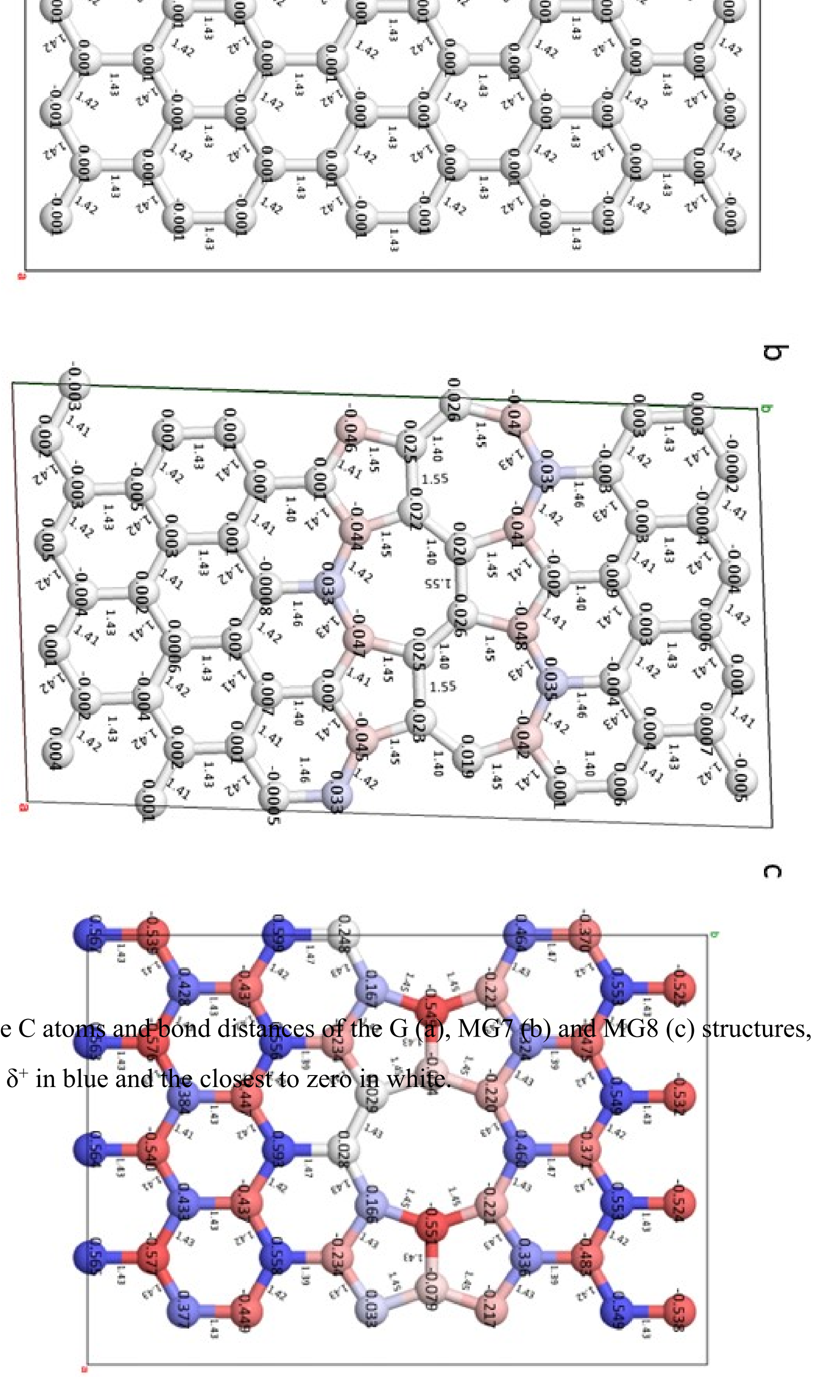

Figure S4. Partial charges (δ) of the C atoms and bond distances of the G (a), MG7 (b) and MG8 (c) structures, being the lowest δ^- in red, the highest δ^+ in blue and the closest to zero in white.

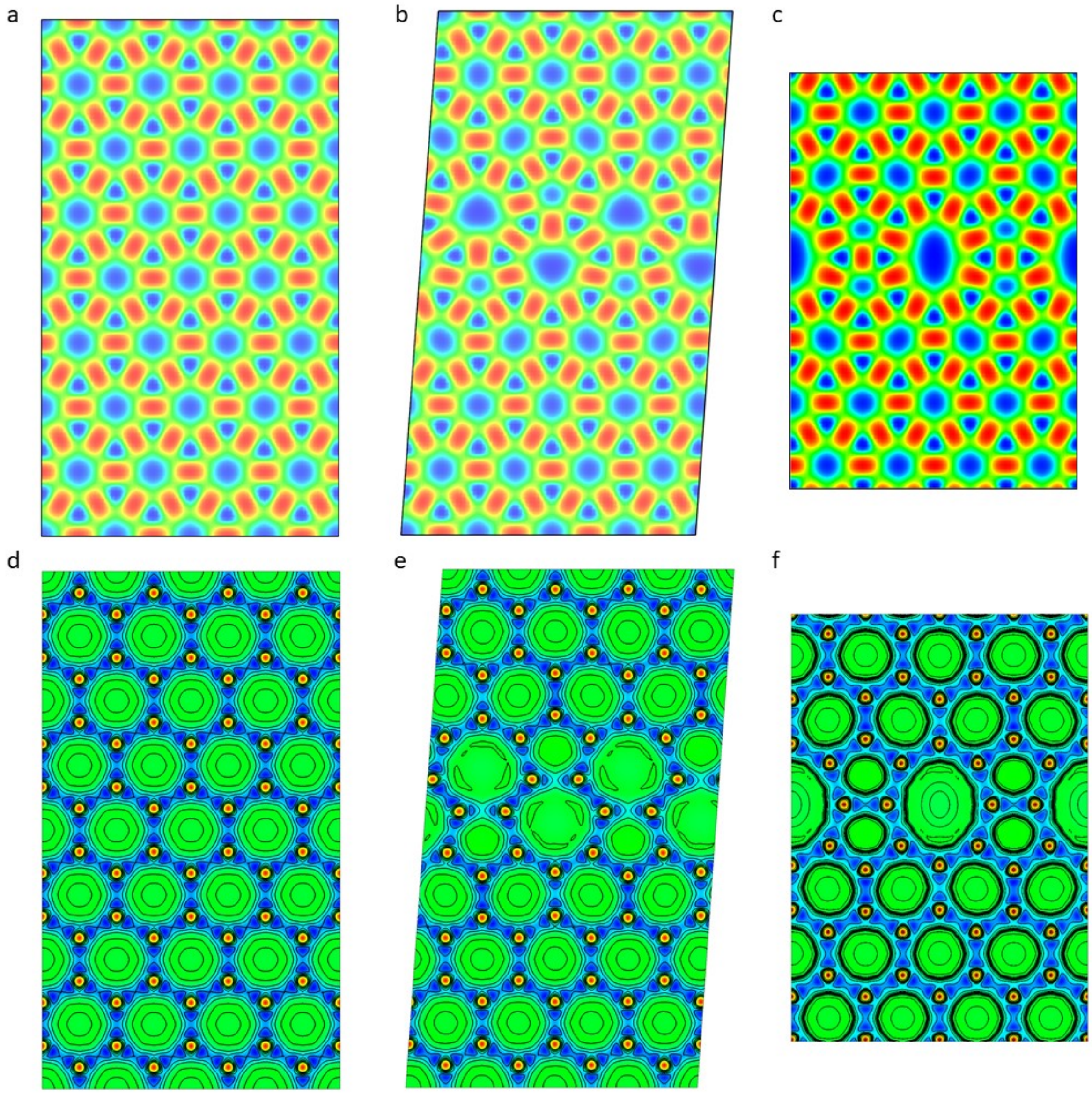

Figure S5. ELF of the section from the *c* direction of G (a), MG7 (b) and MG8 (c) models, where the highest ρ or 1 is in red and the lowest ρ or 0 is in blue. Laplacian of the electron density of the G (d), MG7 (e), and MG8 (f) models in a section taken from the *c* direction. Where $\nabla^2\rho(r_b) < 0$ (blue) or $\nabla^2\rho(r_b) > 0$ (red).

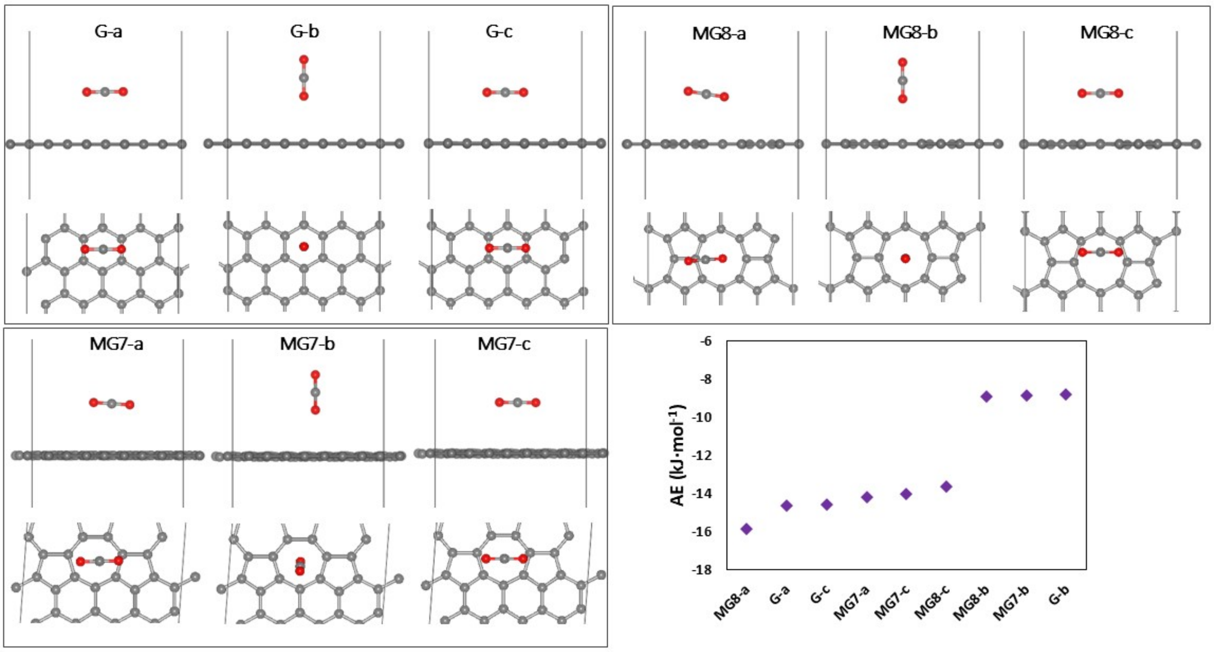

Figure S6. Optimised models and adsorption energies for CO_2 on G, MG7 and MG8 models from different initial arrangements (a, b and c).

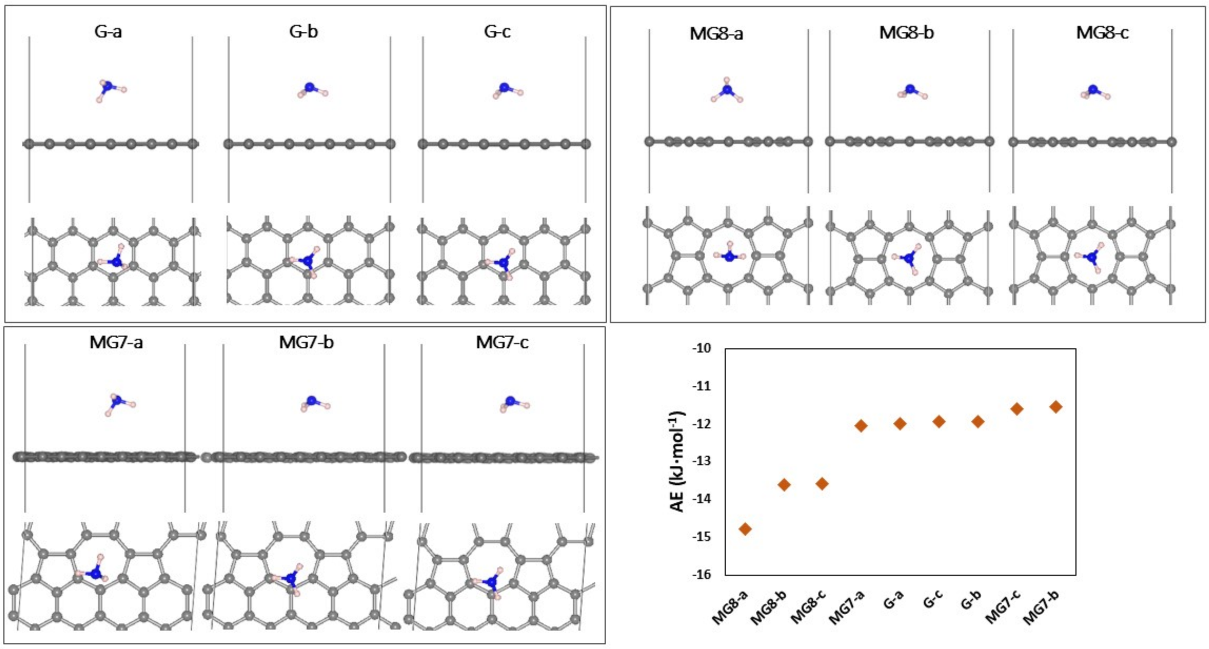

Figure S7. Optimised models and adsorption energies of NH_3 on G, MG7 and MG8 models from different initial arrangements (a, b and c).

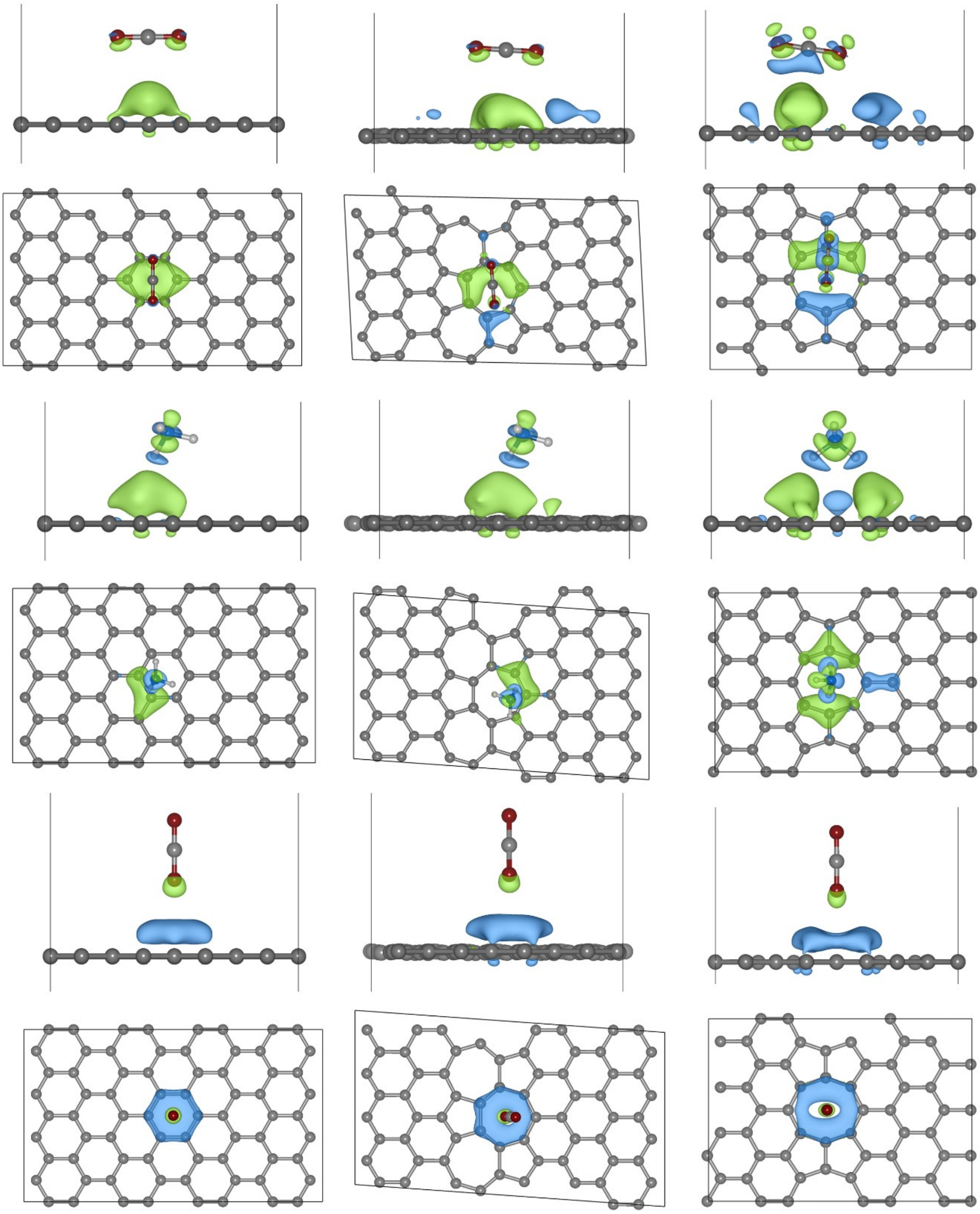

Figure S8. Side and top views of the electron density difference (EDD) maps for CO_2 and NH_3 adsorption on G (first column), MG7 (second column) and MG8 (third column). Each column presents CO_2 interactions (top two panels), followed by NH_3 interactions (central two panels) and the perpendicular CO_2 interactions (bottom two panels). The EDD are visualized through isosurfaces where green regions represent electron accumulation and blue regions indicate electron depletion. The grey spheres represent C atoms in the graphene lattice, while O, N and H atoms are coloured in red, blue and white, respectively. The isosurface value was set to ±0.002 e/Å³ for all plots. This comparison demonstrates how structural defects in graphene influence its interaction with different gas molecules through charge transfer processes.

Model	Molecule	Interaction	BO	d (Å)	δ (e)	Charge product (e^2)	Type
G	CO_2	O67-C51	0.02	3.44	O: -0.35 C: -0.005	0.002	vdW
		C65-C50	0.01	3.65	C: 0.70 C: -0.008	-0.006	vdW
	NH_3	H68-C28	0.02	2.74	H: 0.29 C: -0.01	-0.003	H-bond
		H68-C25	0.01	2.85	H: 0.29 C: -0.006	-0.002	H-bond
MG7	CO_2	O66-C63	0.02	3.39	O: -0.35 C: 0.02	-0.006	vdW
		O66-C63	0.01	3.43	O: -0.35 C: -0.04	0.012	vdW
	NH_3	H68-C25	0.02	2.74	H: 0.29 C: 0.03	0.008	H-bond
		H68-C28	0.02	2.84	H: 0.29 C: -0.04	-0.011	H-bond
MG8	CO_2	C53-C25	0.02	3.29	C: 0.71 C: -0.07	-0.049	vdW
		O54-C14	0.01	3.46	O: -0.35 C: -0.05	0.017	vdW
	NH_3	H56-C25	0.02	2.77	H: 0.29 C: -0.06	-0.018	H-bond
		H54-C14	0.02	2.80	H: 0.29 C: -0.06	-0.018	H-bond
		H54-C35	0.01	2.97	H: 0.29 C: 0.02	0.006	H-bond
		H56-C23	0.01	2.97	H: 0.29 C: 0.03	0.009	H-bond

Table S2. Interactions Between CO_2/NH_3 molecules and G, MG7 and MG8. Bond orders, interatomic distances, partial charges, and charge products are presented for the most significant interactions, computed using the DDEC6 method [64, 65]. For CO_2, interactions are primarily van der Waals in nature, with both carbon and oxygen atoms participating. NH_3 exhibits stronger interactions (H-C) with consistently shorter distances (<3 Å) compared to CO_2-graphene interactions. The charge products reveal the electrostatic character of these interactions (hydrogen bond-like), with both attractive (negative charge product between oppositely charged atoms) and repulsive (positive charge product between similarly charged atoms) components. Notably, the strongest interactions occur at distances between 2.7-3.0 Å with bond orders ranging from 0.0094 to 0.0201, demonstrating the significant role of NH_3 hydrogen atoms in adsorption processes. In the MG8 model, electrostatic forces predominantly govern the diverse hydrogen bonding landscape, where the interplay between charge products (and their dipoles) dictates the strength and nature of the overall binding interactions.

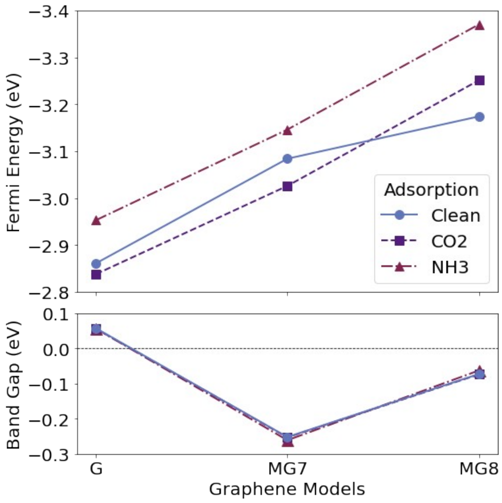

Figure S9. Evolution of Fermi energy and band gap in graphene models upon CO_2 and NH_3 adsorption. Fermi energy shift relative to pristine graphene for clean, CO_2-adsorbed, and NH_3-adsorbed graphene, MG7, and MG8 models. Band gap variation for the same systems. The band gap decreases upon defect introduction and further decreases upon adsorption, indicating a trend towards metallic behavior.

Model	**Fermi Integral**	**Center of Mass (eV)**	**% DOS within 1 eV of Fermi**	**p-orbital contribution**
G	0.4355	-0.6608	0.96%	71.06%
MG7	1.6289	-0.7294	1.90%	70.59%
MG8	2.8466	-0.7772	2.53%	70.97%
CO_2-G	0.4396	-0.4648	1.00%	70.44%
CO_2-MG7	1.6743	-0.5484	2.03%	70.13%
CO_2-MG8	3.0783	-0.7237	2.54%	70.88%
NH_3-G	0.4592	-0.6453	0.97%	70.97%
NH_3-MG7	1.6665	-0.7357	1.86%	70.33%
NH_3-MG8	3.7548	-0.8036	3.00%	70.89%

Table S3. Summary of the Fermi integral, center of mass of the density of states (DOS), percentage of DOS within 1 eV of the Fermi level, and p-orbital contribution calculated for pristine graphene (G) and defective graphene models (MG7 and MG8) with and without adsorbed CO_2 and NH_3 molecules.

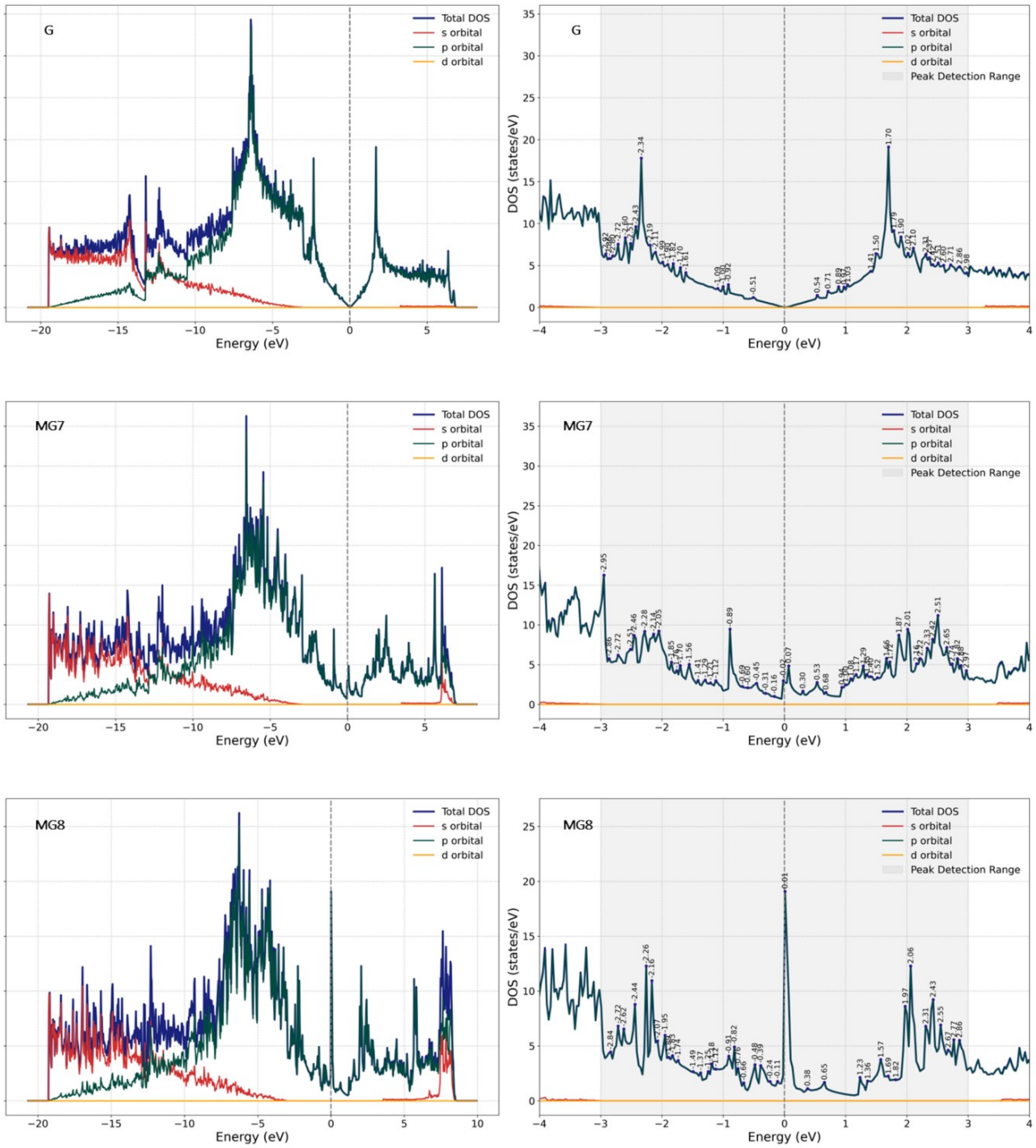

Figure S10. DOS for the G, MG7 and MG8 models for the ranges from -20 to 10 eV (left) and from -4 to 4 eV (right).

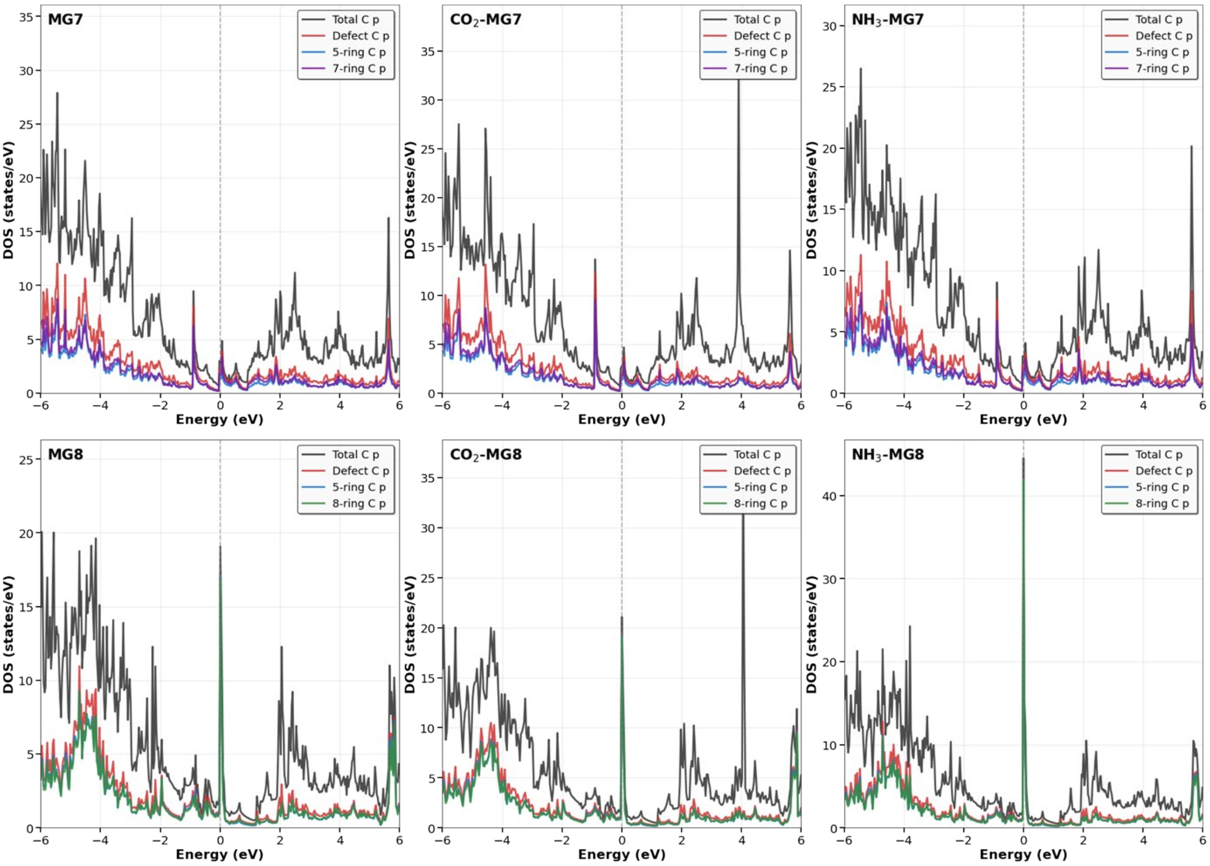

Figure S11. Orbital-projected density of states (PDOS) highlighting the contributions of carbon p-orbitals from defect atoms in MG7 and MG8 before and after adsorption: MG7, CO_2–MG7, NH_3–MG7, MG8, CO_2–MG8, and NH_3–MG8. Total DOS is shown in black, while defect-associated carbon p-orbitals are compared with those of the 5-, 7-, and 8-membered rings. Energy is referenced to the Fermi level (0 eV). The plots confirm that defect-localized p-orbitals dominate the states near the Fermi level and contribute to the enhanced adsorption in defective structures.

The defect-resolved PDOS further highlights the role of localized carbon p-states in MG7 and MG8 (Fig. S9). In MG7, these defect states appear as broader and less intense features near the Fermi level, consistent with its moderate enhancement in adsorption. By contrast, MG8 exhibits a sharp and intense defect p-peak directly at the Fermi level, reflecting a stronger localization that underpins its metallic character and higher reactivity. Upon adsorption, CO_2 shows weak overlap with defect states, mainly through O(p) features around –5 eV and +4 eV (Fig. 6), whereas NH_3 exhibits clearer hybridization with defect-localized C(p) states near –2 eV (Fig. 6). These shifts in intensity and orbital overlap indicate that non-hexagonal ring defects act as electronically active traps, with MG8 providing the most effective sites for charge transfer and molecular activation.